Journal of Electromagnetic Waves and Applications

Analysis of an arbitrary-profile, cylindrical, impedance reflector surface illuminated by an E-polarized complex line source beam

Fadil Kuyucuoglu[a], Taner Oğuzer[b], Ibrahim Avgin[a] & Ayhan Altintas[c]

[a] Electrical and Electronics Engineering Department, Ege University, Izmir, Turkey

[b] Electrical and Electronics Engineering Department, Dokuz Eylul University, Izmir, Turkey

[c] Electrical and Electronics Engineering Department, Bilkent University, Ankara, Turkey
Published online: 24 Dec 2013.

PLEASE SCROLL DOWN FOR ARTICLE

Taylor & Francis
Taylor & Francis Group

Analysis of an arbitrary-profile, cylindrical, impedance reflector surface illuminated by an E-polarized complex line source beam

Fadil Kuyucuoglu[a], Taner Oğuzer[b]*, Ibrahim Avgin[a] and Ayhan Altintas[c]

[a]*Electrical and Electronics Engineering Department, Ege University, Izmir, Turkey;*
[b]*Electrical and Electronics Engineering Department, Dokuz Eylul University, Izmir, Turkey;*
[c]*Electrical and Electronics Engineering Department, Bilkent University, Ankara, Turkey*

Electromagnetic scattering from a cylindrical reflector surface having an arbitrary conic section profile is studied. We assumed an electrically thin layer antenna illuminated by a complex line source in E-polarization mode. Our boundary value formulation, without loss of generality, involves an integral equation approach having impedance-type thin-layer boundary conditions. For simplicity, we also considered both faces of the reflector of the same uniform impedance value. Our computation employs the Method of Analytical Regularization (MAR) technique: the integral equations are converted into the discrete Fourier transform domain yielding two coupled dual series equations, which are then solved by the Fourier inversion and Riemann Hilbert Problem techniques. We demonstrate the accuracy and the convergence behaviors of our numerically solved MAR results that can serve as an accurate benchmark for comparison with widely used results obtained by approximate boundary conditions.

Keywords: reflector surface; numerical modeling; regularization; scattering

1. Introduction

Reflectors with impedance surfaces have important applications in electromagnetics and optics. These structures cannot be simulated using the perfect electric conductor (PEC) boundary condition. Also imperfect micro-mirrors have important usage in the optical systems because the PEC conditions are not valid at optical wavelengths, so suitable boundary conditions have to be defined. Thus, modeling the effect of imperfect metal on the radiation performance is critical.

Many single and dual reflector antenna systems are studied in the literature,[1,2] such as Cassegrain and Gregorian dual systems of various shaped reflector antennas. The main dishes of reflector antennas are generally electrically large. Even at frequencies where the PEC condition for a metal reflector is valid, the regions close to the rim of the reflector should be loaded with the material of proper impedance [3] as to raise the overall radiation performance. If the metal reflector surface has a low conductivity, then the impedance boundary conditions should be imposed. Hence, the impedance boundary conditions are also imposed if there is rust or a thin ice layer on the PEC reflector.

*Corresponding author. Email: taner.oguzer@deu.edu.tr

In the full-wave modeling of electromagnetic scattering problems, the finite-difference time-domain method,[4] and finite element method [5] are commonly used. But especially for larger reflectors, one needs huge number of unknowns to discretize all physical domains around the reflector and has a problem of satisfying the radiation condition. Another formulation is the singular integral equation (SIE) with proper boundary conditions such that the radiation condition is automatically satisfied and the number of unknowns is reduced. Another useful technique is so-called method of moments (MoM) with local or global basis and testing functions. The MoM is already applied to analyze the PEC reflector antennas as in [6,7]. A slightly modified MoM procedure can be applied to the impedance-type boundaries of surfaces.[8] Yet, the MoM convergence is not guaranteed for electrically large structures and also there is a strong dependence on the implementation as such non-realistic computation time may occur. Thus, this modified method is more convenient for small/medium size reflectors.

The exact formulation and the studies of its asymptotic behavior of the impedance reflector problems can also be carried on such as scattering from a 2D circularly curved strip with impedance surfaces.[9,10] It was shown in [11] that if the region close to the reflector rim is loaded by an impedance surface, then overall radiation pattern is improved. The geometrical theory of diffraction is also used for canonical problems of impedance half planes and wedges.[12,13] These studies utilized the plane wave excitation, but the Gaussian beam excitation is also employed for an impedance half-plane problem.[14] Further improvement is obtained by considering the scattering from a cylindrical parabolic impedance surface.[15] Nevertheless, the results of all these studies on impedance surfaces are approximate. Consequently, the beam scattering from the impedance reflector is indeed an important problem and an accurate solution can be useful for generating accurate benchmark data.

A remarkable numerical approach is the analytical regularization (MAR) via SIE's [16], wherein the kernel of the SIE is separated into two parts, the singular part (usually static) and the remainder. Hence, the choice of the global basis functions that are orthogonal eigenfunctions of the singular part enables us to perform analytical inversion using special methods like Riemann Hilbert problem (RHP) technique or Fourier inversion procedure. The remainder leads to the Fredholm second-kind matrix equation system resulting in a convergent numerical solution. This technique is combined with the dual series equation approach that was presented in [17] for a 2D circular screen. A similar approach can be applied to 2D non-circular reflector antenna system or more complicated near-field problems.[18–24] The complex source point (CSP) feed was used to simulate antenna excitation.

Imperfect reflector problem can be analyzed with the SIE-MAR technique. A circular 2-D reflector with a uniform resistivity illuminated by plane waves was studied in [25]. Also non-uniform resistivity version of the same geometry [26] was modeled under the CSP-beam illumination. 2D scattering problem with a non-circular contour with uniform and non-uniform resistive surfaces is studied in [27]. This study is targeted to simulate a parabolic reflector surface excited by a CSP-type directive beam. Then, the H-polarization case of the similar problem is solved in [28] for the non-uniform resistive reflector surface. However unlike,[27] a numerical solution of the elliptic-profile reflectors has been obtained. In the optical frequency range, this study has already an application in the design of micro-size metallic mirrors used in the pump-radiation focusers for the semiconductor lasers.

The MAR technique with dual series equations is also used in the accurate numerical simulation of the resistive or impedance-type flat periodic strip gratings.[29,30] Thanks to

these studies that some reference data are provided as such assessment of the accuracy of any solution can be made. In [31], a similar MAR approach is applied to the light scattering and absorption by a flat infinite grating of thin silver nanostrip.

In this study, 2D non-circular reflector with the impedance surface fed by a CSP directive beam is numerically simulated using SIE-MAR technique together with the dual series formulation. A thin layer boundary conditions presented in [32] is applied using the electrical and magnetic resistivity. With this approach, two systems of dual series equations are obtained. The first one is regularized by the Fourier inversion procedure and the second one by the RHP technique. Then, overall Fredholm second-kind nature is constituted by the remaining parts. Also, we get coupled algebraic equations different from that of a flat case due to the curvature of the reflector surface. We get a convergent solution with a controlled accuracy. We also compared our results with the MoM solutions for a circular profile. We observed that the presented regularized solution has higher accuracy and convergent nature when compared to that of the ordinary MoM and a faster running time is achieved.

We have investigated numerically various radiation characteristics. Here, we used only a single frequency incident wave with suppressed $e^{-i\omega t}$ time convention. Dispersive effects, if any, in the permittivity and permeability of the reflector material can be included by considering the solution in a band of frequencies. Mainly impenetrable-type surface is considered here like a homogeneous good conductor and it almost totally reflects the whole incident power. In the case of dispersion, the reflectivity should change, but then the layer becomes penetrable. This occurs for metals beyond a certain frequency i.e. plasma frequency. In such frequency region, the reflectivity reduces and thin metal layer becomes transparent like a dielectric material with frequency-depended permittivity. In practice, this plasma frequency is very high close to the optical range for all good metals. However, some semiconductors present plasma behavior in the terahertz band which can be realized with today's technology. These semiconductor reflectors are micrometer size which belong to the quasi optical range. Present formulation is capable of solving for reflectors with arbitrary material properties under the thin layer approximation though we concentrated here only on the impenetrable surfaces.

2. Formulation

The 2D reflector surface M can be an arbitrary conic section with a front-fed symmetrical orientation (Figure 1). Both sides of the reflector surface are assumed to have the same uniform impedance. The overall thickness of the reflector is h and it is electrically small i.e. $h \ll \lambda$. Reflector conic section can be elliptic ($0 < e < 1$), parabolic ($e = 1$) or hyperbolic ($1 < e < \infty$) depending on its eccentricity. In making out our formulation, the open arc of the reflector contour M is extended to a complete closed contour C via complementary circular arc S of radius a.

The requirements for a unique solution are the satisfaction of Helmholtz equation, Sommerfeld radiation condition far from the reflector and the source, the impedance boundary condition on M and edge condition. These conditions warrant uniqueness of the solution.[33]

The total tangential electric and magnetic fields on both sides of the thin layer can be stated as

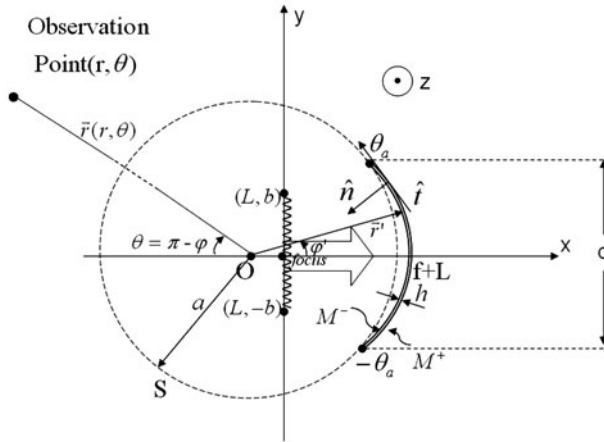$$E_T^{\pm}(\vec{r}) = E_T^{sc\pm}(\vec{r}) + E_T^{in}(\vec{r}) \tag{1}$$

Figure 1.   Problem geometry.

$$H_T^{\pm}(\vec{r}) = H_T^{sc\pm}(\vec{r}) + H_T^{in}(\vec{r}) \tag{2}$$

where $E_T^{sc\pm}$ and $H_T^{sc\pm}$ represent scattered partial fields and E_T^{in}, H_T^{in} represent incident fields. Also, the superscripts "$\pm$" indicate the front ($+$) and back ($-$) reflector faces. The subscript "T" denotes the tangential field. Here, we will try to solve the electric polarization case as such the E-field is taken along the z-direction.

The general impedance boundary conditions for a thin surface can be written as [32];

$$[\vec{E}_T^+(\vec{r}) + \vec{E}_T^-(\vec{r})]/2 = R_T\vec{J}_Z(\vec{r}) + W[\vec{E}_T^+(\vec{r}) - \vec{E}_T^-(\vec{r})] \tag{3}$$

$$[\vec{H}_T^+(\vec{r}) + \vec{H}_T^-(\vec{r})]/2 = S_T\vec{M}_T(\vec{r}) - W[\vec{H}_T^+(\vec{r}) - \vec{H}_T^-(\vec{r})] \tag{4}$$

where R_T and S_T are defined as $R_T = RZ_0$ and $S_T = S/Z_0$. The properties of the thin layer are characterized by the electrical resistivity R_T, the magnetic resistivity S_T, and the cross resistivity W. The free space intrinsic impedance is denoted as Z_0. Also, the electric and magnetic surface currents are given by

$$\vec{J}_Z(\vec{r}) = \hat{n}(\vec{r}) \times [\vec{H}_T^-(\vec{r}) - \vec{H}_T^+(\vec{r})] \tag{5}$$

$$\vec{M}_T(\vec{r}) = -\hat{n}(\vec{r}) \times [\vec{E}_T^-(\vec{r}) - \vec{E}_T^+(\vec{r})] \tag{6}$$

where $\hat{n}$ is the unit normal vector. The above boundary conditions are derived for infinite slab geometries and then they can approximately be used for any smoothly curved surfaces. The aforementioned boundary conditions represent both the penetrable and impenetrable thin layers, yet we consider only the impenetrable case. The general thin layer boundary conditions are also equivalent to the two-sided Leontovich boundary conditions [32] with the surface impedances Z^+ and Z^-. Hence, we can obtain that

$$R_T = \frac{Z^+Z^-}{Z^+ + Z^-}, \quad S_T = \frac{1}{Z^+ + Z^-}, \quad W = \frac{1}{2}\frac{Z^+ - Z^-}{Z^+ + Z^-}, \quad Z^+ + Z^- \neq 0. \tag{7}$$

When the surface impedance of the both sides is equal i.e. $Z^+ = Z^- = Z$, then the cross resistivity W reduces to zero. We used this simplified case for our numerical simulation; a uniform and equal impedance on both sides of the reflector surface. The impedance of the thin reflector surface has been modeled in two different ways in our formulation. First, we assumed a thin layer consisting of a homogeneous and a good conducting metal having a thickness "h" greater than skin depth "δ". The surface impedance is given by $Z = (1 + j)\sqrt{\omega\mu/2\sigma}$ where μ is the permeability and σ is the conductance. The thickness is in between $\delta \ll h \ll \lambda$.

For a general homogeneous material, the permittivity can also be given by $\varepsilon = \varepsilon_0(1 + \sigma/i\omega\varepsilon_0)$ and also the conductivity σ may depend on the frequency as $\sigma = \sigma_0/(1 - i\omega\tau)$ where τ is the relaxation time and σ_0 is the dc conductance. For the frequency range satisfying the high-frequency assumption denoted as $\omega\tau \gg 1$, the permittivity ε is obtained as $\varepsilon = \varepsilon_0(1 - \omega_p^2/\omega^2)$ where ω_p is the plasma frequency.[34] When $\omega < \omega_p$, the incident-wave is strongly reflected by the material and the transmitted wave is attenuated rapidly. But if $\omega > \omega_p$, then the wave inside the material becomes propagating. This dispersion relation is only valid if our high-frequency assumption is satisfied in the neighborhood of $\omega = \omega_p$. Therefore, one can say that good metals present a plasma behavior beyond some frequencies in the optical range. This plasma frequency is directly related to the volume electron density of the material. Therefore, some materials like a semiconductor having lower electron density than that of a metal may have plasma frequency in the terahertz band. For this reason, semiconductors can be used in quasi-optical systems like micrometer size transparent mirrors.

Except for the homogeneous material case, another application is an infinitely thin PEC surface, both faces coated with the same magneto-dielectric thin layer. Thus, the surface impedance of the grounded material layer is given as follows:

$$Z = -i Z_0 \sqrt{\frac{\mu_r}{\epsilon_r}} \tan(\sqrt{\epsilon_r\,\mu_r}k_0 h) \tag{8}$$

where k_0 is the free space wavenumber, h is the thickness of the coating, and ϵ_r and μ_r are the relative permittivity and permeability, respectively. This formula is valid for a thin and high contrast coatings ($k_0 h \ll 1$, $|\epsilon_r\mu_r| \gg 1$). The incident electric field and the magnetic field will be taken as the beam-like form generated by the CSP method given by

$$E_Z^{in}(\vec{r}) = H_0^{(1)}(k_0|\vec{r} - \vec{r}_s|) \quad H_T^{in}(\vec{r}) = \frac{1}{ik_0 Z_0}\frac{\partial E_Z^{in}(\vec{r})}{\partial n} \tag{9}$$

where $\vec{r}$ is the observation vector and $\vec{r}_s$ is the complex source position vector obtained from the real source position vector $\vec{r}_0(x_0, y_0)$ according to the CSP method. Also in this case, the real position coordinates are defined as ($x_0 = L, y_0 = 0$) i.e. feed on-focus case. The complex source position vector is defined as $\vec{r}_s = \vec{r}_0 + i\vec{b}$ that can be written as $\vec{r}_s = (x_0 + ib\cos\beta, y_0 + ib\sin\beta)$ expression where b and β are aperture width and beam-aiming angle, respectively. This incident field expression has two branch points; which dictates that a proper branch cut should be selected. Note that the magnitude of the position vector of the CSP feed is complex-valued, as such $r_s = \sqrt{L^2 - b^2 + i2Lb\cos\beta}$ but, only Re $(r_s) > 0$ branch should be chosen for a physically meaningful case. Also, the complex angle of the CSP feed is given as $\theta_s = \cos^{-1}((L + ib\cos\beta)/r_s)$. The maximum radiation is along $\varphi = \beta$ direction. This field produces a directive beam and it is almost Gaussian near this direction.

3. Derivation of equations

The scattered tangential electric and magnetic fields just on the front and back side of the reflector can be written using the radiation integrals. These radiation integrals are obtained using the auxiliary vector potential-based formulation as given in [18,19]. The overall effects of the electric and magnetic surface currents are seen in these radiation fields given below:

$$E_z^{sc\pm}(\vec{r}) = \mp \frac{1}{2} M_T(\vec{r}) + ik_0 Z_0 \int_M J_Z(\vec{r}')G(k_0|\vec{r}-\vec{r}'|)dl' - \int_M M_T(\vec{r}')\frac{\partial}{\partial n'}G(k_0|\vec{r}-\vec{r}'|)dl' \quad (10)$$

$$H_T^{sc\pm}(\vec{r}) = \mp \frac{1}{2} J_Z(\vec{r}) + \int_M J_Z(\vec{r}')\frac{\partial}{\partial n}G_0(k_0|\vec{r}-\vec{r}'|)dl' + \frac{ik_0}{Z_0}\int_M M_T(\vec{r}')\cos(\xi(\vec{r})$$

$$- \xi(\vec{r}'))G(k_0|\vec{r}-\vec{r}'|)dl' + \frac{1}{ik_0 Z_0}\int_M M_T(\vec{r}')\frac{\partial^2}{\partial l \partial l'}G(k_0|\vec{r}-\vec{r}'|)dl' \quad (11)$$

where the free space Green's function is $G(k_0|\vec{r}-\vec{r}'|) = i/4H_0^{(1)}(k_0|\vec{r}-\vec{r}'|)$. When the observation point approach to the surface of the reflector from inner and outer region, terms $\pm 1/2 J_z$ and $\pm 1/2 M_T$ indicate the vicinity of singularity in the radiation integrals. Then, applying the initially defined boundary conditions with the total fields for both sides, one can obtain the following electric-field integral equations (EFIE).

$$ik_0 Z_0 \int_M J_Z(\vec{r}')G(k_0|\vec{r}-\vec{r}'|)dl' - \int_M M_T(\vec{r}')\frac{\partial}{\partial n'}G(k_0|\vec{r}-\vec{r}'|)dl' + E_z^{in}(\vec{r}) = R_T J_Z(\vec{r}), \quad \vec{r} \in M \quad (12)$$

$$\int_M J_Z(\vec{r}')\frac{\partial}{\partial n}G(k_0|\vec{r}-\vec{r}'|)dl' + \frac{ik_0}{Z_0}\int_M M_T(\vec{r}')\cos(\xi(\vec{r})-\xi(\vec{r}'))G(k_0|\vec{r}-\vec{r}'|)dl'$$

$$+ \frac{1}{ik_0 Z_0}\int_M M_T(\vec{r}')\frac{\partial^2}{\partial l \partial l'}G(k_0|\vec{r}-\vec{r}'|)dl' + H_T^{inc}(\vec{r}) = S_T M_T(\vec{r}), \quad \vec{r} \in M \quad (13)$$

In the above EFIEs, the formulation has more complicated form for a curved layer than that of a flat case because the curved layer constitutes a coupled integral equation system. The flat periodic impedance grating problem is treated in [29,30] using Floquet series-based mode matching approach to get an accurate solution.

We made a regularized numerical solution different from the conventional MoM discretization solution. The MoM algorithm is not usually fast enough when we solve large reflector surfaces with high accuracy. In our computation, to obtain a convergent, accurate, and faster algorithm, we used two different MAR regularization procedure for the first and the second integral equations together with the Fourier inversion procedure and the RHP technique, respectively.

Suppose, now that the arbitrary conic section profile can be characterized by parametric equations in terms of the polar angle $x = x(\varphi)$, $y = y(\varphi)$ on M where $-\theta_a < \varphi < \theta_a$. We denote the differential lengths in the tangential direction as $\partial l = a\beta(\varphi)\,\partial\varphi$. Here, $\beta(\varphi) = r(\varphi)/(a\cos\gamma(\varphi))$, $r(\varphi)$ is the length of the position vector defined on M (metal part) starting from the origin, $\xi(\varphi)$ is the angle between the normal and the x-direction, $\gamma(\varphi)$ is the angle between the normal and the radial direction, and a is the radius of the auxiliary circle. We set surface-current densities $\tilde{J}_Z$ and $\tilde{M}_T$ to zero on S (slot). Thus, we can modify the above EFIEs on the complete contour C made of M and S as such the corresponding angle φ spans the whole period that is $\varphi \in [0, 2\pi]$. Multiplying

each term with $\beta(\varphi)$ in both the integral equations in (12) and (13) and defining $X(\varphi) = \tilde{J}_Z(\varphi)\beta(\varphi)$, we can obtain the following dual equation system from the first one

$$ik_0 a Z_0 \int_0^{2\pi} X(\varphi')G(k_0|\vec{r}(\varphi) - \vec{r}'(\varphi')|)\beta(\varphi)\mathrm{d}\varphi' - \int_0^{2\pi} \tilde{M}_T(\varphi')\frac{\partial}{\partial n'}G(k_0|\vec{r}(\varphi)$$

$$- \vec{r}'(\varphi')|)a\beta(\varphi)\beta(\varphi')d\varphi' + E_z^{in}(\varphi)\beta(\varphi) = R_T X(\varphi), \quad \varphi \in M \quad (14)$$

$$0 = X(\varphi) \quad \varphi \in S \quad (15)$$

The second one produces the following dual equation system,

$$\int_0^{2\pi} X(\varphi')\frac{\partial}{\partial n}G(k_0|\vec{r}(\varphi) - \vec{r}'(\varphi')|)a\beta(\varphi)d\varphi' + \frac{ik_0 a}{Z_0}\int_0^{2\pi} \tilde{M}_T(\varphi')\cos(\xi(\varphi)$$

$$- \xi(\varphi'))G(k_0|\vec{r}(\varphi) - \vec{r}'(\varphi')|)\beta(\varphi)\beta(\varphi')d\varphi' + \frac{a}{ik_0 Z_0}\int_0^{2\pi} \tilde{M}_T(\varphi')\frac{\partial^2}{\partial l \partial l'}G(k_0|\vec{r}(\varphi)$$

$$- \vec{r}'(\varphi')|)\beta(\varphi)\beta(\varphi')d\varphi' + H_T^{inc}(\varphi)\beta(\varphi) = S_T \tilde{M}_T(\varphi)\beta(\varphi), \quad \varphi \in M \quad (16)$$

$$0 = \tilde{M}_T(\varphi) \quad \varphi \in S \quad (17)$$

To discretize the set of dual equation systems given in (14), (15) and (16), (17), the entire domain exponents are used. The surface current densities are expanded as follows

$$X(\varphi) = \frac{2}{i\pi Z_0}\sum_{n=-\infty}^{\infty} x_n e^{in\varphi}, \quad \tilde{M}_T(\varphi) = \frac{2}{i\pi}\sum_{n=-\infty}^{\infty} m_n e^{in\varphi} \quad \varphi \in C. \quad (18)$$

The incident electric and magnetic field expressions $E_z^{in}\beta(\varphi)$ and $H_T^{inc}\beta(\varphi)$ on C can be represented by Fourier series (FS) coefficients $\{e_n^{inc}\}_{n=-\infty}^{\infty}$ and $\{z_n^{inc}\}_{n=-\infty}^{\infty}$, respectively, where "$e$" is not to be mixed with the Euler number e. Kernel functions in the integral equation systems given above should be expanded into double FS whose coefficients calculated numerically. To perform more economic and easier computation, we extract out singularities. So we add to and subtract from original kernels similar functions of well behaved in singularity that are given at the full auxiliary circle having the radius a. The subtracted function forms can be written as

$$H_1(\varphi, \varphi') = H_0^{(1)}(k_0 R) - H_0^{(1)}(2k_0 a \sin|(\varphi - \varphi')/2|) \quad (19)$$

$$H_2(\varphi, \varphi') = \frac{\partial H_0^{(1)}(k_0 R)}{\partial n'}a\beta(\varphi') - k_0 a \sin(|(\varphi - \varphi')/2|)H_1^{(1)}(2k_0 a \sin|(\varphi - \varphi')/2|) \quad (20)$$

$$H_3(\varphi, \varphi') = \frac{\partial H_0^{(1)}(k_0 R)}{\partial n}a\beta(\varphi) + k_0 a \sin(|(\varphi - \varphi')/2|)H_1^{(1)}(2k_0 a \sin|(\varphi - \varphi')/2|) \quad (21)$$

$$H_4(\varphi, \varphi') = \beta(\varphi')\beta(\varphi)\cos[\xi(\varphi) - \xi(\varphi')]H_0^{(1)}(k_0 R) - \beta^2(\varphi)H_0^{(1)}\left(2k_0 a \sin\frac{|\varphi - \varphi'|}{2}\right). \quad (22)$$

These new functions show regular behavior as $\varphi' \to \varphi$. The double FS coefficients of these functions can be written $h_{nm}^1, h_{nm}^2, h_{nm}^3$, and h_{nm}^4 in the same order. Also the

curvatures of M and S are matched at the connection points so the functions $H_1(\varphi, \varphi')$, $H_4(\varphi, \varphi')$, and their first derivatives with respect to φ and φ' are continuous functions on the whole C. Their second derivatives with respect to φ and φ' have only logarithmic singularity and hence belong to L_2. Therefore, their FS coefficients decay as $O(|n|^{-1/5-\varepsilon}|m|^{-1/5-\varepsilon})$ on the curve C. The other two functions $H_2(\varphi, \varphi')$ and $H_3(\varphi, \varphi')$, and their derivatives have no singularity. So, we expect them to decay faster. The corresponding FS coefficients can be computed by FFT algorithm efficiently and this provides us to solve reasonably larger geometries.

After substituting all the above functions in the Fourier series form into the integral equation (14) and (15) system and then evaluating the integrals, we obtain

$$
x_m + \underbrace{\frac{k_0 a}{R_T}\frac{\pi Z_0}{2}\sum_n x_n \sum_p Q^1_{p-m}h^1_{p(-n)}}_{\sum_n x_n A^1_{mn}} + \underbrace{\frac{k_0 a}{R_T}\frac{\pi Z_0}{2}\sum_n x_n J_n(k_0 a)H^{(1)}_n(k_0 a)Q^1_{n-m}}_{\sum_n x_n A^2_{mn}}
$$

$$
+ \underbrace{\frac{i}{R_T}\frac{\pi Z_0}{2}\sum_n m_n \sum_p Q^1_{p-m}h^2_{p(-n)}}_{\sum_n m_n B^1_{mn}}
$$

$$
+ \underbrace{\frac{k_0 a}{R_T}\frac{i\pi Z_0}{2}\sum_n m_n (J'_n(k_0 a)H^{(1)}_n(k_0 a) + J_n(k_0 a)H^{(1)\prime}_n(k_0 a))Q^1_{n-m}}_{\sum_n m_n B^2_{mn}}
$$

$$
= \underbrace{\left(\frac{i}{R_T}\frac{\pi Z_0}{2}\right)\sum_n e^{inc}_n Q^1_{n-m}}_{T_m} \tag{23}
$$

where $Q^1_{n-m} = \frac{1}{2\pi}\int_{-\theta_a}^{\theta_a}\beta(\varphi)e^{i(n-m)\varphi}d\varphi$. The IE system given in (14) and (15) are transformed to the dual-series form and it can be readily inverted by Fourier inversion technique as shown previously for decoupled single equation.[27] Here, R_T is the regularization parameter that should not be zero to form the Fredholm second-kind behavior of the equation.

Thus, the IE system given in (16) and (17) is also converted to the dual-series form using the FS expansions of all functions. Using the asymptotic behavior of cylindrical functions, we can reduce this dual series equation to a well-known canonical form as presented in Appendix. The obtained canonical dual series equation can be written as

$$
\sum_n m_n |n| e^{in\varphi} = -\sum_p m_p \underbrace{[i\pi|p|^2 J_p(k_0 a)H^{(1)}_p(k_0 a) - |p|]}_{\Delta_p} e^{ip\varphi} - i\pi \sum_p e^{ip\varphi} p \sum_n m_n n h^1_{p(-n)}
$$

$$
+ i\pi(k_0 a)^2 \sum_p e^{ip\varphi}\sum_n \bar{\beta}_{p-n}m_n J_n(k_0 a)H^{(1)}_n(k_0 a)
$$

$$
+ i\pi(k_0 a)^2 \sum_p e^{ip\varphi}\sum_n m_n h^4_{p(-n)} + \pi(k_0 a)\sum_p e^{ip\varphi}\sum_n x_n h^3_{p(-n)}
$$

$$
- (k_0 a)^2 \pi \sum_p x_p (J'_p(k_0 a)H^{(1)}_p(k_0 a) + J_p(k_0 a)H^{(1\prime)}_p(k_0 a))e^{ip\varphi}
$$

$$
+ \pi k_0 a Z_0 \sum_p z^{inc}_p e^{ip\varphi} + ik_0 a 2 Z_0 S_T \sum_p e^{ip\varphi}\sum_n m_n Q^2_{p-n}, \quad \varphi \in M \tag{24}
$$

$$\sum_n m_n e^{in\varphi} = 0, \quad \varphi \in S \tag{25}$$

Then, the resultant matrix equation is written as explained in Appendix:

$$m_m + \underbrace{\sum_n m_n \Delta_n \tilde{T}_{mn}}_{\sum_n m_n C_{mn}^1} + \underbrace{i\pi \sum_n m_n n \sum_p p h_{p(-n)}^1 \tilde{T}_{mp}}_{\sum_n m_n C_{mn}^2}$$

$$-\underbrace{i\pi (k_0 a)^2 \sum_n m_n J_n(k_0 a) H_n^{(1)}(k_0 a) \sum_p \bar{\beta}_{p-n} \tilde{T}_{mp}}_{\sum_n m_n C_{mn}^3} - \underbrace{i(k_0 a)^2 \pi \sum_n m_n \sum_p \tilde{T}_{mp} h_{p(-n)}^4}_{\sum_n m_n C_{mn}^4}$$

$$+ \underbrace{\pi (k_0 a)^2 \sum_n x_n \tilde{T}_{mn} ((J_n'(k_0 a) H_n^{(1)}(k_0 a) + J_n(k_0 a) H_n^{(1)\prime}(k_0 a)))}_{\sum_n x_n D_{mn}^1}$$

$$- \underbrace{\pi k_0 a \sum_n x_n \sum_p \tilde{T}_{mp} h_{p(-n)}^3}_{\sum_n x_n D_{mn}^2} - \underbrace{i k_0 a 2 Z_0 S_T \sum_n m_n \sum_p \tilde{T}_{mp} Q_{p-n}^2}_{\sum_n m_n C_{mn}^5} = \underbrace{(\pi k_0 a) Z_0 \sum_n \tilde{T}_{mn} z_n^{\text{inc}}}_{E_m} \tag{26}$$

where $\beta^2(\varphi)$ and $\beta(\varphi)$ are represented by FS coefficients $\bar{\beta}_t$'s and Q_t^2 in FS form with the sub-indices "t". In equation (26), the MAR method is used for the regularization. The DSE given in equations (24) and (25) are solved by the RHP technique. This is equivalent to the inversion of the more singular part of the original operator by semi-inversion procedure. Finally, an algebraic equation system is also obtained with the other remaining parts.

The algebraic equations in (23) and (26) can be considered as the coupled equation system. Then, combining them leads the following matrix equation:

$$\underbrace{\begin{bmatrix} x_m \\ m_m \end{bmatrix}}_{y_m} + \underbrace{\begin{bmatrix} A_{mn}^1 + A_{mn}^2 & B_{mn}^1 + B_{mn}^2 \\ D_{mn}^1 + D_{mn}^2 & C_{mn}^1 + C_{mn}^2 + C_{mn}^3 + C_{nm}^4 + C_{mn}^5 \end{bmatrix}}_{Z_{mn}} \underbrace{\begin{bmatrix} x_n \\ m_n \end{bmatrix}}_{y_n} = \underbrace{\begin{bmatrix} T_m \\ E_m \end{bmatrix}}_{P_m}. \tag{27}$$

Large index assumptions for cylindrical functions enable us to prove that $\sum_{m,n=-\infty}^{\infty} |Z_{mn}|^2 < \infty$. By the similar treatment, we can find that $\sum_{m=-\infty}^{\infty} |P_m|^2 < \infty$ provided that the branch cut associated with the CSP aperture does not cross the reflector contour M. In this case, the matrix equation system given in (27) is of the Fredholm second kind. Hence, the Fredholm theorems guarantee the existence of the unique exact solution and the convergence of approximate numerical solution can be obtained with progressively larger sizes N_{tr}.

4. Radiation characteristics

The scattering characteristics of an impedance reflector illuminated by the E-polarized CSP feed are determined by the far-zone field radiation pattern. Since the CSP satisfies the radiation condition, we can conveniently include its radiation pattern in the total field,

$$E_z(\vec{r}) = [\phi_{in}(\varphi) + \phi_{sc}(\varphi)] \left(\frac{2}{i\pi k r}\right)^{1/2} e^{ikr} \tag{28}$$

$$\phi_{in}(\varphi) = e^{kb\cos(\varphi-\beta)} \tag{29}$$

$$\phi_{sc}(\varphi) = \left(-\frac{k_0 a}{4}\right)\left\{Z_0 \int_0^{2\pi} X(\varphi')e^{-ikr'\cos(\varphi-\varphi')}d\varphi'\right.$$
$$\left. - \int_0^{2\pi}\tilde{M}_{\tan}(\varphi')\cos(-\varphi+\varphi'-\gamma')e^{-ikr'\cos(\varphi-\varphi')}\beta(\varphi')d\varphi'\right\} \tag{30}$$

It is assumed that the feed is located at the focus point and the surface current densities $X(\varphi)$ and $\tilde{M}_{\tan}(\varphi)$ are expanded as the FS form given in the Equation (18). The total power radiated by the CSP feed in the presence of reflector is

$$P_{rad}(R_T, S_T) = \frac{1}{Z_0 \pi k_0}\int_0^{2\pi}|\phi_{in}(\varphi)+\phi_{sc}(\varphi)|^2 d\varphi. \tag{31}$$

The total radiated power is a function of the reflector resistivities R_T and S_T as well as the geometric parameters of the source and the reflector. Then, the overall directivity function can be obtained as

$$D(\varphi) = 2\pi\frac{|\phi_{in}(\varphi)+\phi_{sc}(\varphi)|^2}{\int_0^{2\pi}|\phi_{in}(\varphi)+\phi_{sc}(\varphi)|^2 d\varphi} \tag{32}$$

The forward directivity value can be obtained from this function by choosing as $\varphi = \pi$.

5. Numerical results

We checked our formulation against various parameters when reproducing the radiation characteristics. To compare our results, we have also calculated the fields using MoM. The MoM for a circular profile is applied here using the volume equivalence theorem-based approach. The thin circular reflector layer is discretized by circular volumetric meshes and then point-wise collocation is used. The MoM is in fact slower in our circular profile and even slower for an arbitrary profile. When we compute the Fourier coefficients of our defined functions, we used Fast Fourier Transform (FFT) algorithm with 2048-points. The FFT approach enables us to solve electrically large reflectors within a reasonable time. To generate all our numerical results we have used a desktop PC core i-5 computer with 4 GB RAM and Windows 7 operating system.

The accuracy and convergence of our formulation can be checked using the norm expression of the relative error in the directivity of an overall reflector antenna as $\Delta D = (|D^{N_{tr}+1} - D^{N_{tr}}|).(D^{N_t})^{-1}$ where N_{tr} is the truncated value of the matrix equation system. Figure 2(a) demonstrates the directivity variation with respect to N_{tr} for the MAR and the MOM cases. This figure is obtained for a highly conductive surface close to the PEC one. The directivity for both cases converges to the same value as truncation number increases. Figure 2(b) shows relative error in directivity i.e. ΔD vs. truncation number. Even if we expect the worse convergence case in the MAR due to the a very small surface impedance making the first IE system badly-conditioned, we obtain that the MAR-based results converge better than the MOM results as such we get two-digit differences in the accuracy.

Figure 3 presents the variation of the directivity and its relative error vs. N_{tr} for different eccentricities (*e*). In Figure 3(a), the directivity becomes larger for parabola and
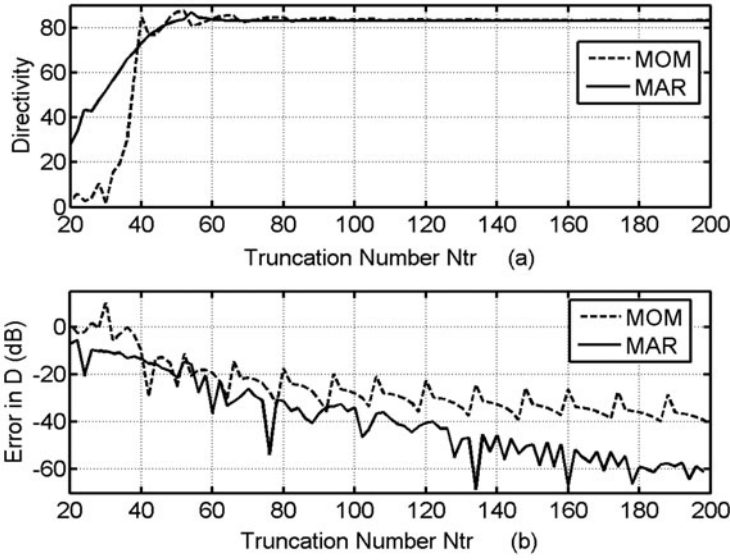
Figure 2.   (a) Directivity, (b) directivity error comparisons as functions of truncation number for the MAR and the MOM cases; the other parameters are $f = 20\lambda$, $d = 25\lambda$, $e = 0$(circle), kb = 5, $\sigma = 1.03 \times 10^7$ S/m, $R_T/Z_0 = (2.6 - 2.6i) \times 10^{-5}$, and $S_T Z_0 = (4.8 + 4.8i) \times 10^3$.
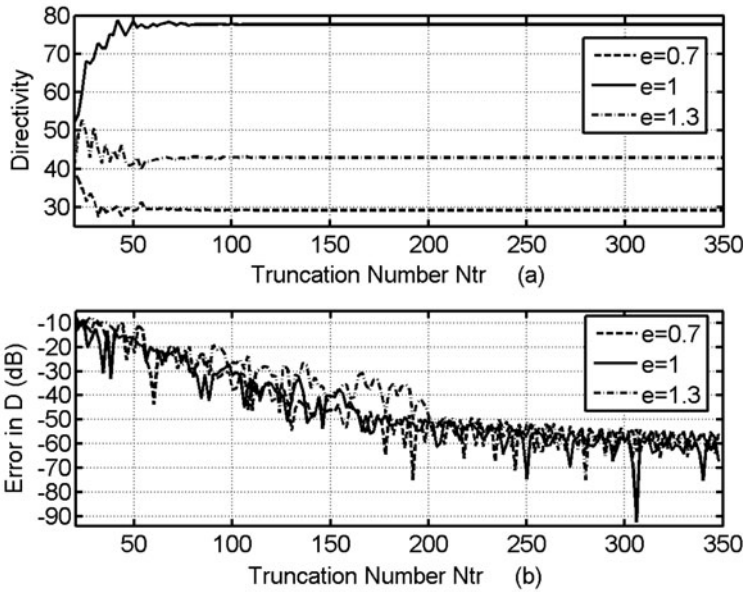

Figure 3.   (a) Directivity, (b) directivity error comparisons as functions of truncation number with different eccentricity factors for the MAR cases. The problem parameters are given as $Z = -i \times 0.25\ Z_0$, $f = 10\lambda$, $d = 20\lambda$, and kb = 5.

Figure 4. Relative error in (a) electric current density (*J*) and (b) magnetic current density (*M*) as functions of truncation number with different eccentricity factors for the MAR case. The problem parameters are given as $Z = -i \times 0.25\ Z_0$, $f = 10\lambda$, $d = 20\lambda$, and kb = 5.
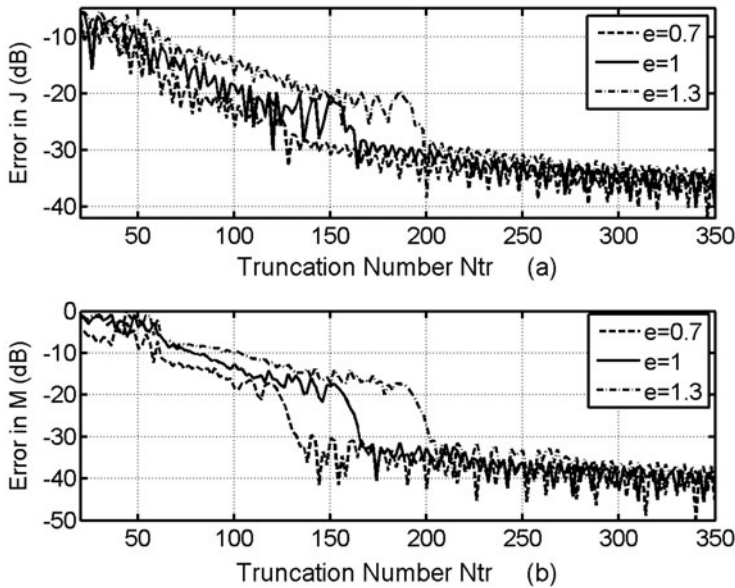
it converges for various *e* values. In Figure 3(b), the relative error variation in directivity with the truncation number N_{tr} is given for three different eccentricities. We obtain numerical convergence for all eccentricities for sufficiently large truncation number.

The relative error in electric current density (*J*) and magnetic current density (*M*) are demonstrated in Figure 4(a) and (b), respectively. The relative errors for *J* and M imply the following maximum norm expressions that can be written as $\Delta J = \max |x_n^{N_t+1} - x_n^{N_{tr}}|(\max |x_n^{N_{tr}}|)^{-1}$ and $\Delta M = \max |m_n^{N_{tr}+1} - m_n^{N_{tr}}|(\max |m_n^{N_{tr}}|)^{-1}$. The relative errors exhibit a decaying nature for each eccentricity and we notice that the larger eccentricity converges more slowly. This is due to the overall scale of our geometry becoming larger when completing the circular parts.

Figure 5(a) shows the radiation pattern comparison results of a highly conductive surface obtained by the method: the MAR, the MOM, and the PEC. We clearly see that while the MAR solution almost overlaps with the PEC result, the MOM result deviates in the backside region. Yet, by decreasing the mesh size in the MoM, backside pattern of the MOM converges very slowly to the PEC result not shown in the figure. In Figure 5(b), we computed the physical optics (PO) for the impedance surface and while it is an asymptotic technique, compared to our MAR calculation, it yields consistent results. We show the radiation patterns in Figure 5(c) obtained by our MAR for homogeneous material-type reflector surfaces. The results show that obtained patterns do not change appreciably by varying realistic material conductivities, besides we can see a small deviation only for a very low conductivity at the back side lobes.

The radiation patterns with different eccentricities are shown in Figure 6 for various surface impedances. We can see that the parabola has the lowest main beam width as expected. Also, as the surface impedance increases from $-i0.025Z_0$ to $-i0.5Z_0$,

deviations occur from the PEC case especially at the back side lobe region. This type of impedance physically means that the coated PEC surfaces are lossless dielectric material and support surface waves. Hence, we say that the increasing surface waves produces higher edge diffraction mechanism leading to an increasing radiation level for larger impedances.

We also computed another type of electrically and magnetically coated PEC reflector with lossy surfaces. For example in Figure 7, we show radiation patterns for different electric-type materials with various thicknesses and the deviations from the PEC case increase with the increasing thickness. And this deviation is higher for the electric material having $\varepsilon_r = 20 - 3i$ than that of $\varepsilon_r = 3 - 20i$.

Similar radiation plots are given in Figure 8 for magnetic materials of different thicknesses. The deviations from the PEC case can be distinguished even better when compared to that of shown in Figure 7, covering almost all radiation regions. Also, deviations from the PEC increase as thickness is increased. The magnetic material having complex permeability μ_r, we get larger deviation for the larger imaginary part.

Figure 9(a) shows directivity vs. eccentricity for altered impedance values. We obtain clearly a maximum directivity in the parabolic case ($e = 1$) for each curve. Directivity reduces as impedance increases. Figure 9(b) shows the directivity vs. η factor for different d values under the fixed f/d ratio. Let us define $Z = -i\eta Z_0$ where
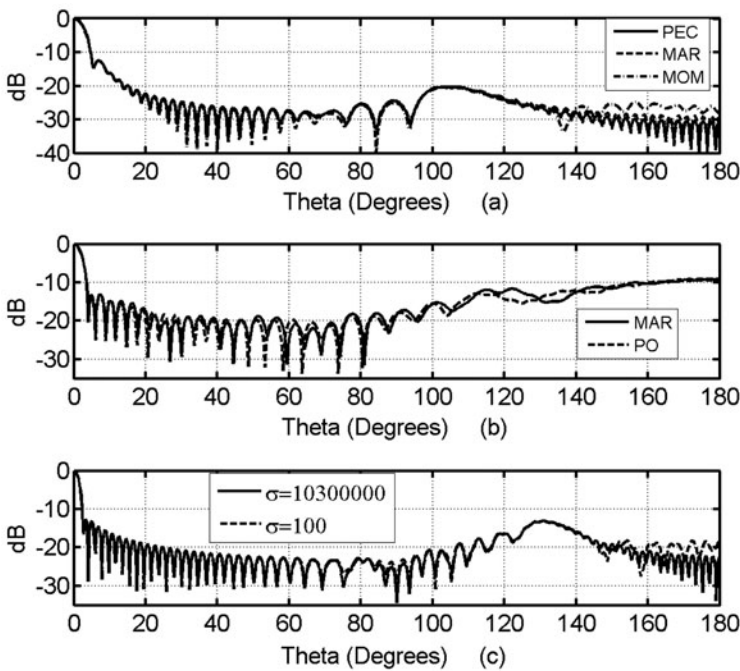

Figure 5. Normalized electric field magnitude pattern comparisons (a) the MAR and the MOM solution for a metal with $\sigma = 1.03 \times 10^7$ S/m and the PEC, the other parameters are $f = 20\lambda$, $d = 25\lambda$, e = 0 (circle), kb = 5, $R_T/Z_0 = (2.6 - 2.6i) \times 10^{-5}$, and $S_T Z_0 = (4.8 + 4.8i) \times 10^3$ (b) Pattern comparison between the MAR and the PO for the problem parameters given as $Z = -i \times 0.25\ Z_0$, $f = 10\lambda$, $d = 20\lambda$, and kb = 3 and $e = 1$(parabola) (c) Pattern comparison for various surface conductivity for the MAR method. The problem parameters given as $f = 20\lambda$, $d = 30\lambda$, and kb = 5 and $e = 1$ (parabola).
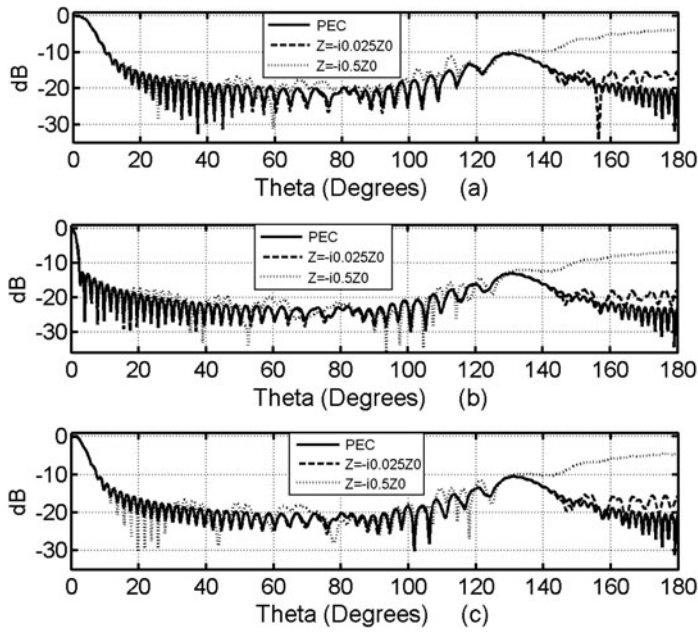
Figure 6. Normalized electric field magnitude pattern comparisons of the PEC and impedance sheets with different impedance values for different eccentricity values (a) e = 0.7, (b) e = 1, and e = 1.3, other parameters are f = 20λ, d = 30λ, and kb = 5.
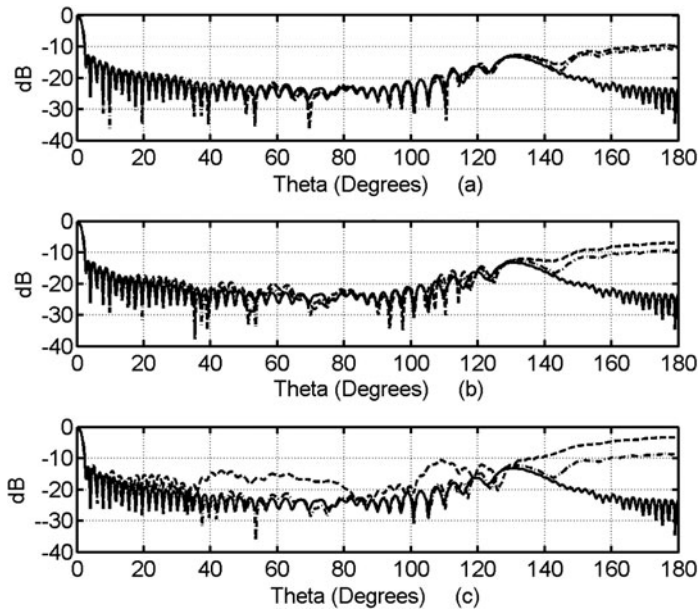
Figure 7. Normalized electric field magnitude pattern comparisons of the PEC coated with different electric-type material for thicknesses (a) 0.03λ, (b) 0.04λ, and (c) 0.05λ. Solid curve is for the PEC, dashed curve is for ε_r = 20–3i, and dotted curve is for ε_r = 3–20i, the other parameters are f = 20λ, d = 30λ, e = 1 (parabola), and kb = 5.
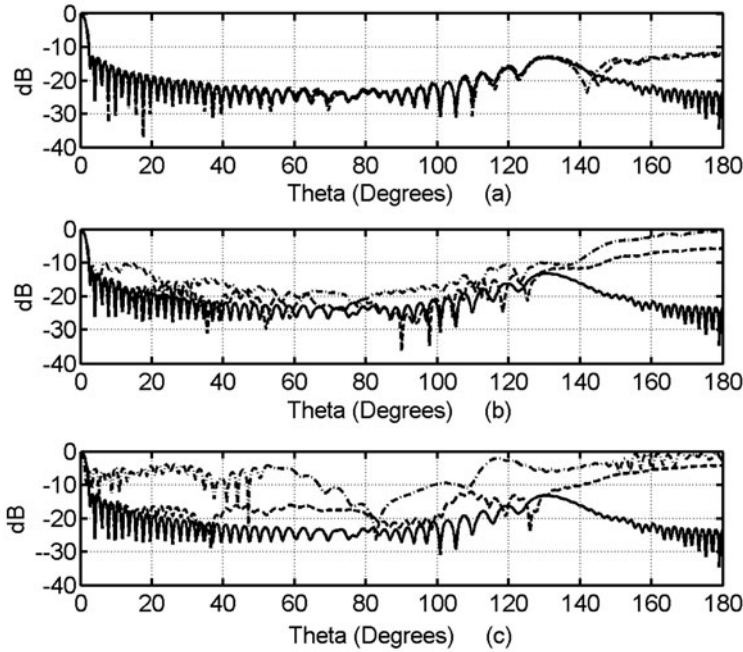
Figure 8. Normalized electric field magnitude pattern comparisons of the PEC coated with different magnetic-type material for thicknesses (a) 0.001λ, (b) 0.005λ, and (c) 0.01λ. Solid curve is for the PEC, dashed curve is for $\mu_r = 20-3i$ and dotted curve is for $\mu_r = 3-20i$, other parameters are $f = 20\lambda$, $d = 30\lambda$, $e = 1$ (parabola), and kb = 5.
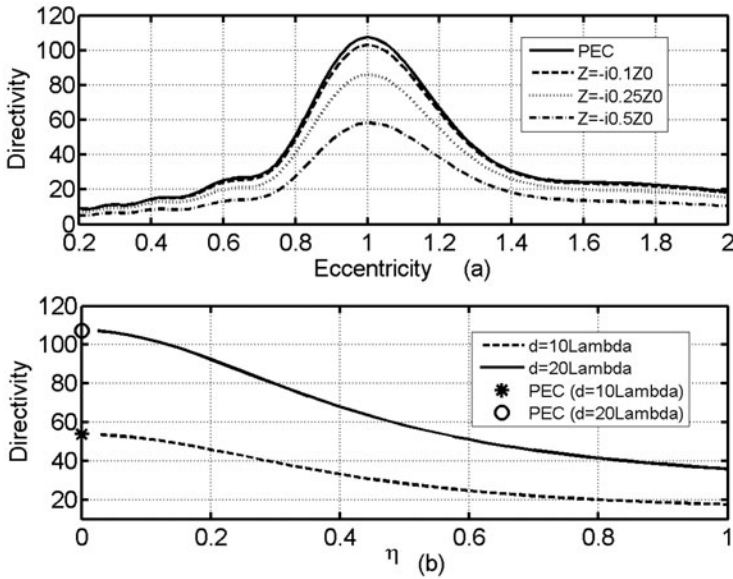

Figure 9. (a) Forward directivity comparisons of the PEC and different impedance sheets with different Z values vs. eccentricity. The other parameters are kb = 3, $f/d = 0.5$, and $d = 20\lambda$ (b) Forward directivity comparisons vs. η. The other parameters are $e = 1$, kb = 3, $d = 20\lambda$, and $f/d = 0.5$.

$\eta = 0$ describes the PEC case as marked on the plots. It is seen from the graphs that as $\eta \to 0$, two curves converge to two marked points. The PEC case gives the maximum directivity as expected but if we increase η, the directivity decreases.

6. Conclusions

We have studied wave scattering from the 2-D arbitrary-profile impedance reflector surface using the SIE. Two different systems of dual series equations are obtained for thin layer boundary conditions; afterwards they are solved by analytical regularization techniques. Hence, obtained results can provide accurate data to compare with that of the other approximate techniques. The reflector surface is illuminated by a directive beam created by a complex source. The effect of the impedance of the reflector surface on the radiation performance of an overall reflector antenna system is analyzed and we obtain excellent agreement against other available numerical results.

References

[1] Scott CR. Modern methods of reflector antenna analysis and design. Boston (MA): Artech House; 1990P.

[2] Bhattacharyya AK. High-frequency electromagnetic techniques: recent advances and applications. New York (NY): Wiley; 1995.

[3] Bucci Ovidio M, Franceschetti Giorgio. Rim loaded reflector antennas. IEEE Trans. Antennas Propag. 1980;28:297–305.

[4] Hower GL, Olsen RG, Earls JD, Scheider JB. Inaccuracies in numerical calculation of scattering near to natural frequencies. IEEE Trans. Antennas Propag.. 1993;41:982–986.

[5] Volakis JL, Chatterjee A, Kempel LC. Review of the finite-element method for three-dimensional electromagnetic scattering. J. Opt. Soc. Am. A. 1994;11(4):1422–1433.

[6] Barclay MR, Rusch WVT. Moment-method analysis of large, axially symmetric reflector antennas using entire domain functions. IEEE Trans. Appl. 1991;39:491–496.

[7] Heldring A, Rius JM, Ligthart LP, Cardama A. Accurate numerical modeling of the TARA reflector system. IEEE Trans. Appl. 2004;52:1758–1766.

[8] Glisson Allen W. Electromagnetic scattering by arbitrarily shaped surfaces with impedance boundary conditions. Radio Science. 1992;27:935–943.

[9] Idemen M, Buyukaksoy A. High-frequency surface currents induced on a perfectly conducting cylindrical reflector. IEEE Trans. Antennas Propag. 1984;32(5):501–507.

[10] Akduman I, Buyukaksoy A. Asymptotic expressions for the surface currents induced on a cylindrically curved impedance strip. IEEE Trans. Antennas Propag. 1995;43:453–463.

[11] Bucci MO, Massa Di G, Catello S. Control of reflector antennas performance by rim loading. IEEE Trans. Appl. 1981;29:773–779.

[12] Tiberio R, Pelosi G, Manara G. A uniform GTD formulation for the diffraction by a wedge with impedance faces. IEEE Trans. Antennas Propag. 1985;33:867–873.

[13] Volakis JL. A uniform geometrical theory of diffraction for an imperfectly conducting half-plane. IEEE Trans. Antennas Propag. 1986;34:172–180.

[14] Umul YZ. Scattering of a Gaussian beam by an impedance half-plane. J. Opt. Soc. Am. A. 2007;24:3159–3167.

[15] Umul YZ. Scattering of a line source by a cylindrical parabolic impedance surface. J. Opt. Soc. Am. A. 2008;25:1652–1659.

[16] Nosich AI. Method of analytical regularization in the wave-scattering and eigenvalue problems: foundations and review of solutions. IEEE Transactions on AP Mag. 1999;42:34–49.

[17] Oğuzer T, Altintas A, Nosich AI. Accurate simulation of reflector antennas by the complex source-dual series approach. IEEE Trans. Antennas Propag. 1995;43:793–801.

[18] Oğuzer T, Nosich AI, Altintas A. E-Polarized beam scattering by an open cylindrical PEC strip having arbitrary conical-section profile. Microwave Opt Technol Lett. 2001;31:480–484.

[19] Oğuzer T, Nosich AI, Altintas A. Analysis of an arbitrary profile cylindrical reflector antenna, H-polarization case. IEEE Trans. Antennas Propag. 2004;52:3156–3162.

[20] Oğuzer T. Analysis of circular reflector antenna covered by concentric dielectric radome. IEEE Trans. Antennas Propag. 2001;49:458–463.

[21] Oğuzer T, Altintas A. Analysis of the 2D nonconcentric reflector antenna-in-radome system: E-Polarization case. J. Electromagn. Waves Appl. 2005;19:2093–2111.

[22] Oğuzer T, Altintas A. Analysis of the nonconcentric reflector antenna in radome system by the iterative reflector antenna and radome interaction. J. Electromagn. Waves Appl. 2007;21:57–70.

[23] Boriskina SV, Nosich AI, Altintas A. Effect of the imperfect flat earth on the vertically-polarized radiation of a cylindrical reflector antenna. IEEE Trans. Appl. 2007;48:285–292.

[24] Yurchenko VB, Altintas A, Nosich AI. Numerical optimization of a cylindrical reflector-in-radome antenna system. IEEE Trans. Antennas Propag. 1999;47:668–673.

[25] Nosich AI, Okuno Y, Shiraishi T. Scattering and absorption of E and H-polarized plane waves by a circularly curved resistive strip. Radio Sci. 1996;31:1733–1742.

[26] Nosich AI, Yurchenko VB, Altintas A. Numerically exact analysis of a two dimensional variable-resistivity reflector fed by a complex point source. IEEE Trans. Antennas Propag. 1997;45:1592–1601.

[27] Oğuzer T, Altintas A, Nosich AI. Integral equation analysis of an arbitrary profile and varying-resistivity cylindrical reflector illuminated by an E-polarized complex source-point beam. J. Opt. Soc. Am. A. 2009;26:1525–1532.

[28] Oğuzer T, Altıntaş A, Nosich AI. Analysis of the elliptic-profile cylindrical reflector with a varying resistivity using the complex source and dual-series approach: H-polarization case. Opt. Quantum Electron J. 2013;45:797–812.

[29] Zinenko TL, Nosich A I, Okuno Y. Plane wave scattering and absorption by resistive-strip and dielectric-strip periodic gratings. IEEE Trans. Antennas Propag. 1998;46:1498–1505.

[30] Zinenko T L, Nosich A I. Plane wave scattering and absorption by flat grating of impedance strips. IEEE Trans. Antennas Propag. 2006;54:2088–2095.

[31] Zinenko TL, Marciniak M, Nosich A I. Accurate analysis of light scattering and absorption by an infinite flat grating of thin silver nanostrips in free space using the method of analytical regularization. IEEE J. Sel. Top. Quantum Electron. 2013;19:9000108/8.

[32] Bleszynski E, Bleszynski M, Jaroszewicz T. Surface integral equations for electromagnetic scattering from impenetrable and penetrable sheets. IEEE Trans. Appl. 1993;35:14–25.

[33] Colton D, Kress R. Integral equation method in scattering theory. New York (NY) Wiley; 1983.

[34] Ashcroft NW, David Mermin N. Solid state physics. Philadelphia, PA: Saunders College; 1976.

Appendix

(1) The 2D Green's function for the free space and its first-order normal derivatives are given as follows,

$$G(\vec{r}, \vec{r}') = \frac{i}{4} H_0^{(1)}(k_0 R) \tag{A1}$$

$$\frac{\partial G(\vec{r}, \vec{r}')}{\partial n'} = \nabla' G . \hat{a}_{n'} \tag{A2}$$

where $\nabla' G$ and $\hat{a}_{n'}$ parameters are defined as

$$\nabla' G(\vec{r}, \vec{r}') = \underbrace{-\frac{i}{4} k_0 H_1^{(1)}(k_0 R)}_{\partial G/\partial R} \left(\frac{\partial R}{\partial x'} \hat{a}_x + \frac{\partial R}{\partial y'} \hat{a}_y \right). \tag{A3}$$

$$\hat{a}_{n'} = \frac{\frac{\partial x(\varphi')}{\partial \varphi'}\hat{a}_y - \frac{\partial y(\varphi')}{\partial \varphi'}\hat{a}_x}{\rho(\varphi')}, \tag{A4}$$

Then the first-order normal derivatives with respect to the source and observation coordinates are:

$$\frac{\partial G}{\partial n'} = \frac{ik_0}{4} H_1^{(1)}(k_0 R) \left[\frac{-\frac{\partial y(\varphi')}{\partial \varphi'}(x(\varphi) - x(\varphi')) + (y(\varphi) - y(\varphi'))\frac{\partial x(\varphi')}{\partial \varphi'}}{\rho(\varphi')R} \right], \tag{A5}$$

$$\frac{\partial G}{\partial n} = -\frac{ik_0}{4} H_1^{(1)}(k_0 R) \left[\frac{-\frac{\partial y(\varphi)}{\partial \varphi}(x(\varphi) - x(\varphi')) + (y(\varphi) - y(\varphi'))\frac{\partial x(\varphi)}{\partial \varphi}}{\rho(\varphi)R} \right]. \tag{A6}$$

Here $k_0 = \omega\sqrt{\varepsilon_0\mu_0}$; $H_{0(1)}^{(1)}(\,\cdot\,)$ is the zero- (first-) order Hankel function of the first kind; $\vec{r}$ and $\vec{r}'$ are the vectors from origin to the observation and source points, respectively; $R = |\vec{r} - \vec{r}'|$; and $\rho(\varphi')$ is the Jacobian of the contour C defined as $\rho(\varphi') = a\beta(\varphi')$.

(2) The following dual series equations are in a special form called the canonical form.

$$\sum_{p=-\infty}^{\infty} m_p |p| e^{ip\varphi} = \sum_{p=-\infty}^{\infty} f_p e^{ip\varphi}, \quad \theta_{ap} < |\varphi - \varphi_0| \le \pi, \tag{A7}$$

$$\sum_{p=-\infty}^{\infty} m_p e^{ip\varphi} = 0, \quad |\varphi - \varphi_0| < \theta_{ap}. \tag{A8}$$

Here, there is a circular contour in the complex plane which has an aperture. The second series are defined on this aperture with respect to the central direction φ_0 and the aperture width $2\theta_{ap}$. The first one is defined on the remaining region. By applying the RHP technique to this dual series equation on the circular contour, one can find the following solution

$$m_m = \sum_{p=-\infty}^{\infty} f_p \underbrace{(-1)^{m+p}\, e^{i(p-m)\varphi_0}\, T_{mp}(-\cos\theta_{ap})}_{\tilde{T}_{mp}} \tag{A9}$$

where $T_{mp}(\,\cdot\,)$ functions are special functions of Legendre polynomials. The detailed solution is given in [16]. In our front fed case, $\theta_{ap} = \pi - \theta_a$ and $\varphi_0 = \pi$. Here, the f_p coefficients are obtained by comparing the right-hand side of (24). The f_p coefficients have the additional serial expansions and a change in the order of the summations is required to find the final serial result.